Chemical Science

ROYAL SOCIETY OF CHEMISTRY

EDGE ARTICLE

View Article Online
View Journal | View Issue

Cite this: *Chem. Sci.*, 2025, **16**, 17736

All publication charges for this article have been paid for by the Royal Society of Chemistry

Received 17th June 2025
Accepted 26th August 2025

DOI: 10.1039/d5sc04436g

rsc.li/chemical-science

GSH-responsive magnetic imaging for *in situ* monitoring of tumor chemodynamic therapy

Jun Lu,†[ab] Zhongyao Jiang,†[ab] Xinyu Chen,[a] Wei Zhang,*[a] Ping Li,[a] Yue Tang,*[c] Wen Zhang,[a] Hui Wang[a] and Bo Tang*[ab]

Chemodynamic therapy (CDT) is a promising treatment modality that utilizes highly toxic hydroxyl radicals (˙OH) to kill tumor cells *in situ*. However, real-time monitoring of drug distribution and therapeutic response remains a challenge, hindering the optimization of personalized treatment regimens. Here, we developed a glutathione (GSH)-responsive nanoreactor (FA-Mn NR), with integrated magnetic resonance imaging (MRI) functionality for self-enhanced CDT. The nanoreactor undergoes GSH-triggered Mn^{2+} release, which simultaneously functions as an MRI contrast agent and catalyzes hydrogen peroxide (H_2O_2) to produce additional ˙OH, thereby achieving synergistic CDT amplification. The study demonstrates a theranostic platform combining GSH-responsive imaging guidance with enhanced therapeutic efficacy, presenting a novel approach for cancer therapy.

Introduction

Current clinical cancer treatments, such as surgery, chemotherapy, and radiotherapy, play vital roles in antitumor therapy. However, the effectiveness is often compromised by limitations such as intervention timing, systemic side effects, and drug resistance.[1,2] Chemodynamic therapy (CDT) has emerged as an innovative strategy that utilizes the Fenton-like reaction to convert endogenous hydrogen peroxide (H_2O_2) into highly toxic hydroxyl radicals (˙OH) for tumor eradication.[3–5] Unlike photodynamic therapy (PDT) and photothermal therapy (PTT), CDT operates independently of external energy sources, thereby overcoming the limitations associated with tissue light penetration depth, which is a promising anti-tumor strategy.[6–8] Importantly, real-time monitoring of drug distribution and therapeutic progression is crucial to optimize personalized treatment regimens and achieve precision therapy.[9] Currently, advanced imaging techniques such as photoacoustic imaging (PAI), photothermal imaging (PTI), and magnetic resonance imaging (MRI) have been developed to visualize and assess tumor tissues.[10–12] Nevertheless, the design of smart contrast agents capable of minimizing background interference while simultaneously enabling imaging-guided anti-tumor therapy remains a significant challenge.[13]

The tumor microenvironment (TME) provides a suitable environment for tumor cell proliferation and plays a pivotal role in facilitating metastasis, invasion, and multidrug resistance.[14,15] Therein, glutathione (GSH) stands out as the most abundant thiol-based antioxidant, serving as a critical defense mechanism against reactive oxygen species (ROS) and xenobiotic drugs.[16–20] While normal cells typically maintain GSH concentrations of 1–2 mM, cancer cells exhibit markedly elevated levels (~10 mM).[21,22] This GSH overexpression poses a significant challenge for CDT, as it scavenges therapeutic ROS, enhances tumor cell antioxidant capacity.[23–26] Paradoxically, GSH-rich environment offers a unique biochemical switch, enabling the design of tumor-selective, GSH-responsive systems for precision imaging and therapy.[27–29]

Transition metal ions such as Mn^{2+}, Cu^{+}, and Co^{2+} have been widely explored as catalytic agents in Fenton-like reactions due to redox-active properties.[30,31] Notably, many of these ions exhibit multivalent states, enabling redox cycling that depletes GSH while simultaneously enhancing CDT efficacy—a strategy with significant therapeutic potential. Considering oxidation and imaging contrast,[32] Mn element was selected as the catalytic ion to develop Mn(III)-doped nanomaterials targeting tumor cells for CDT with MRI guidance. Specifically, FA-Mn NRs internalized by tumor cells react with GSH to release Mn^{2+}, which depletes the antioxidant defense system and serves dual roles: (i) acting as an MRI contrast agent for real-time monitoring, and (ii) catalyzing H_2O_2 to produce ˙OH, thereby amplifying oxidative stress and enabling MRI-guided therapeutic feedback. Furthermore, to address the insufficient endogenous H_2O_2 levels in tumors for efficient CDT, glucose

[a]College of Chemistry, Chemical Engineering and Materials Science, Collaborative Innovation Center of Functionalized Probes for Chemical Imaging in Universities of Shandong, Key Laboratory of Molecular and Nano Probes, Ministry of Education, Institute of Biomedical Sciences, Shandong Normal University, Jinan 250014, P. R. China. E-mail: tangb@sdnu.edu.cn; zhangwei@sdnu.edu.cn

[b]Laoshan Laboratory, Qingdao 266237, P. R. China

[c]Department of Emergency Medicine, Shandong Provincial Clinical Research Center for Emergency and Critical Care Medicine, Qilu Hospital of Shandong University, Jinan, 250014, P. R. China. E-mail: yuetang0531@hotmail.com

† These authors contributed equally to this work.

oxidase (GOx) was integrated into the system. GOx catalyzes intratumoral glucose oxidation to generate H_2O_2 *in situ*, which supplies substrates for Fenton-like reaction and initiates starvation therapy (*via* glucose depletion), synergistically enhancing anti-tumor outcomes (Scheme 1).

Results and discussion

Synthesis and characterization of Mn(III)-doped nanoparticles

In order to realize chemodynamic therapy under GSH-responsive imaging monitoring, we designed and synthesized FA-Mn NR and GOx-FA-Mn NR. The nanoparticles were synthesized through a straightforward fabrication process. Transmission electron microscopy (TEM) revealed that Mn NRs exhibited spherical morphology with a uniform size distribution (Fig. 1a and b). Subsequently, surface functionalization with folic acid and GOx induced distinct morphological transformations, as evidenced by increased diameters and irregular architectures in both FA-Mn NR and GOx-FA-Mn NR (Fig. S1). X-ray energy spectrum analysis (EDS) confirmed the characteristic signals of C, N, O and Mn contained in FA-Mn NR, indicating the successful doping of manganese ions (Fig. S2). X-ray photoelectron spectroscopy (XPS) further validated the conclusion (Fig. 1c). In addition, the analysis of XPS spectra shows that the valence state of manganese in FA-Mn NR is mainly trivalent, accounting for about 50.2% (Fig. 1d). UV-vis absorption spectra of FA-Mn NR and GOx-FA-Mn NR displayed characteristic folic acid absorption bands at 280 nm, confirming effective folate doping (Fig. 1e and f). Fluorescence spectra showed minimal excitation/emission peak shifts post-functionalization, indicating preserved optical properties in FA-Mn NRs (Fig. S3). Thermogravimetric analysis (TGA) revealed exceptional thermal stability for both Mn NR and FA-Mn NR (Fig. S4).

GSH depletion and ROS generation by Mn(III)-doped nanoparticles

As the predominant intracellular antioxidant, GSH plays a critical role in mitigating oxidative stress, thereby potentially compromising CDT efficacy. Previous studies suggest that high-valent metal ions can oxidize GSH to its dimeric form (GSSG), disrupting cellular redox homeostasis. To quantify this effect, we employed Ellman's reagent to measure GSH levels in reaction systems containing Mn(III)-doped nanoparticles.[33,34] As expected, Mn(III)-nanoparticles demonstrated efficient GSH depletion, significantly reducing GSH concentrations in the reaction system (Fig. 2a, S5 and S6). GSH consumption is an inherent characteristic of Mn(III)-doping nanoparticle.

To characterize Mn^{2+} release, we conducted time-dependent release assays by incubating FA-Mn NR with GSH, followed quantitative analysis of supernatant Mn content. Results revealed that FA-Mn NR undergoes reduction-triggered manganese ions liberation in the presence of glutathione, with rapid ion release observed within 15 minutes followed by progressively increased manganese ions in the supernatant over extended periods (Fig. S7). Moreover, XPS analysis of the precipitates derived from FA-Mn NR after 30 min GSH reaction revealed a Mn(III) content of 37.88% (Fig. S8). By extending the reaction time, the content of manganese(III) in the precipitate further decreased to 23.65% (Fig. 2b), collectively confirming

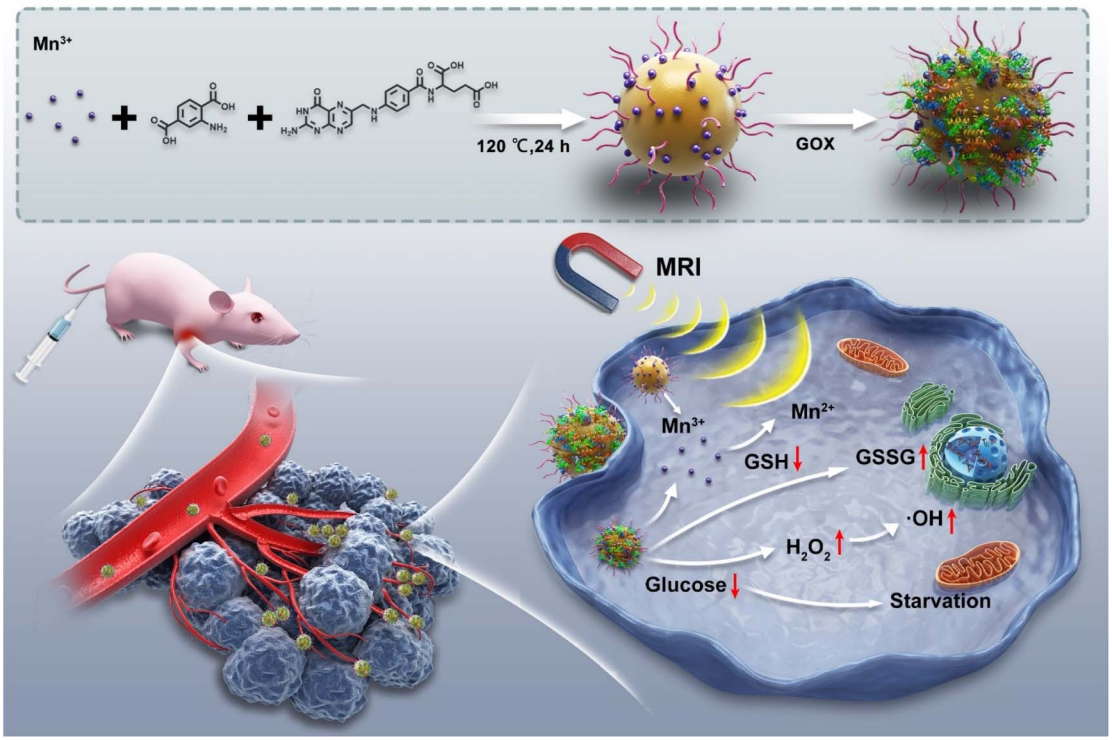

Scheme 1 Schematic of the proposed mechanism of Mn(III)-doped nanoparticles synergistic enhancement of CDT under MRI monitoring.

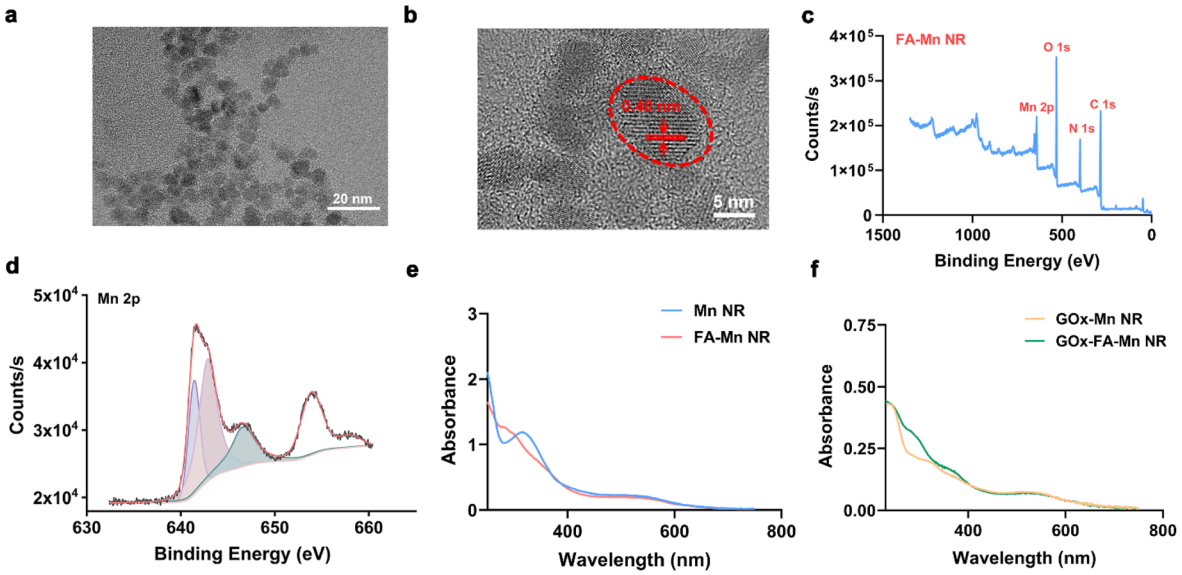

Fig. 1 The characterization of Mn(III)-doped nanoparticles. (a and b) TEM images of Mn NR. (c) XPS spectrum of FA-Mn NR. (d) High-resolution Mn 2p XPS spectrum of in FA-Mn NR. (e) UV-vis absorption spectra of Mn NR and FA-Mn NR. (f) UV-vis absorption spectra of GOx-Mn NR and GOx-FA-Mn NR.

redox-driven dissolution that underpin subsequent sustained Fenton-like reaction.

GOx is a highly efficient enzyme that can catalyze the intracellular decomposition of glucose into gluconic acid and hydrogen peroxide. Significantly, the above processes can replenish raw materials for the Fenton-like reaction and affect the supply of nutrients to cells and initiate starvation therapy. To verify H_2O_2 generation, we employed our previously developed NP-Golgi probe,[35] which exhibits concentration-dependent fluorescence enhancement at 560 nm. Fluorescence spectroscopy revealed systems containing GOx-FA-Mn NRs and glucose demonstrated significant 560 nm fluorescence intensification, confirming enzymatic H_2O_2 production (Fig. 2c). Concurrently, gluconic acid accumulation acidified the

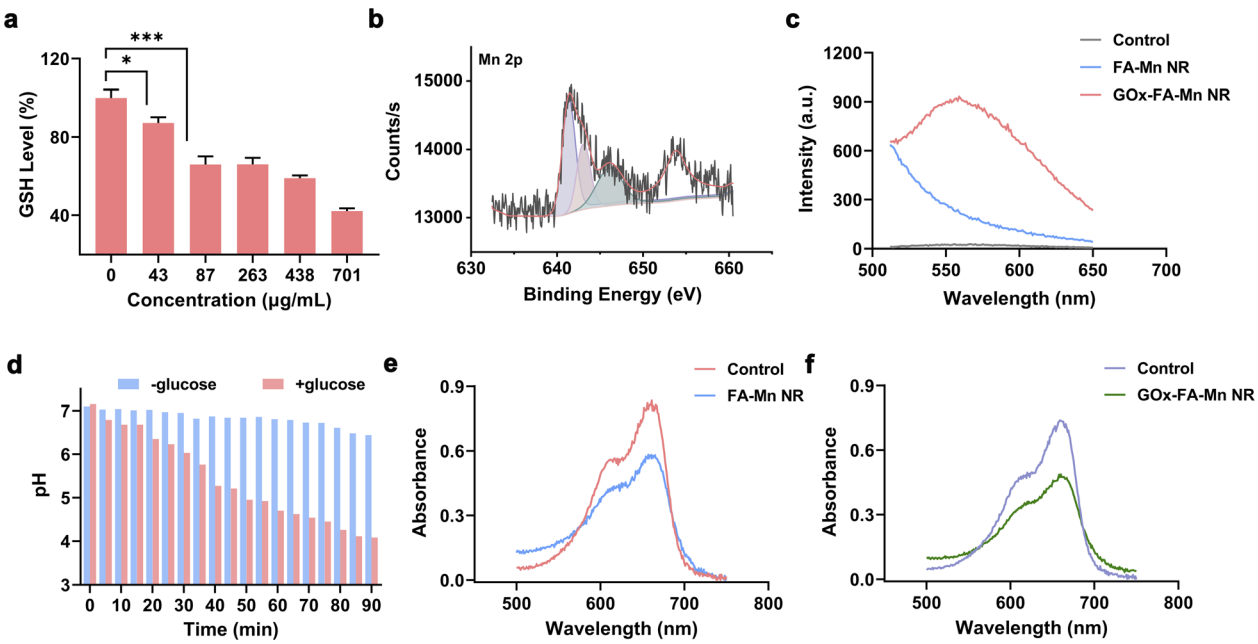

Fig. 2 GSH depletion and ROS generation. (a) GSH consumption in FA-Mn NR systems at varying concentrations. (b) Mn 2p XPS spectrum of FA-Mn NR post-GSH treatment. (c) Fluorescence spectra of NP-Golgi probes in different reaction system. (d) Time-dependent pH changes across experimental groups. (e) UV-vis spectra of MB aqueous solution treated with FA-Mn NR plus H_2O_2. (f) UV-vis spectra of MB aqueous solution treated with GOx-FA-Mn NR plus glucose. Data are expressed as the mean ± SD. *p < 0.05; ***p < 0.001. The significance was determined by a Student's t-test.

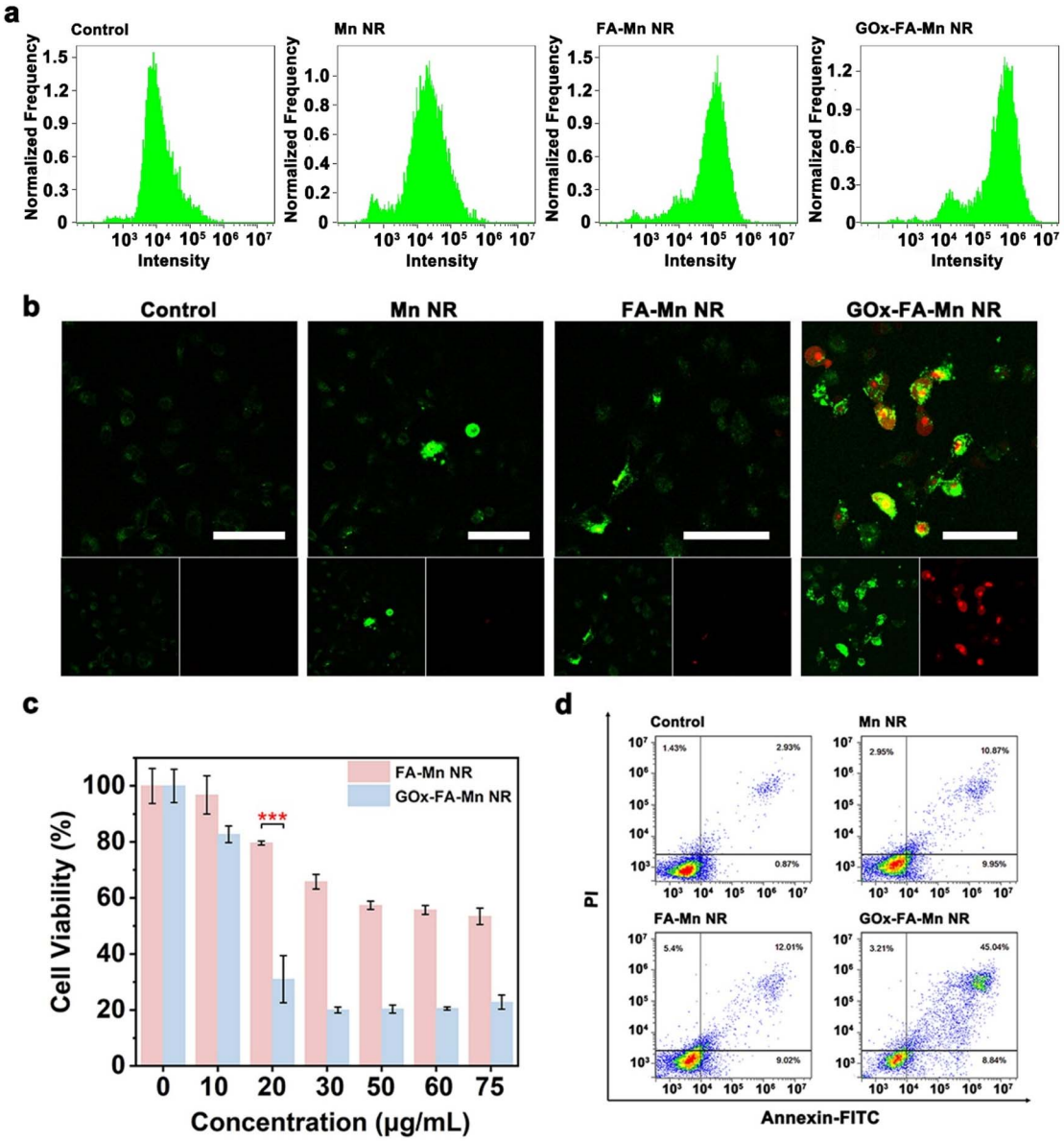

Fig. 3 Intracellular ROS detection and death assessment. (a) The fluorescence intensity of DCF in cells was measured and analyzed by flow cytometry. (b) The fluorescence images of Annexin V-FITC/PI-stained cells exposed to Mn(III)-doped nanoparticles (green: Annexin V-FITC, red: PI). (c) Cell viability after FA-Mn NR and GOx-FA-Mn NR treatments. (d) Flow cytometry analysis of cells incubated with different nanoparticle. Scale bar: 100 μm. Data are expressed as the mean ± SD. ***$p < 0.001$. The significance was determined by a Student's t-test.

reaction microenvironment,[36] with pH decreasing from 7.1 to 4.1 within 90 minutes (Fig. 2d). Extended reaction times (300–900 minutes) yielded further acidification, as evidenced by pH indicator paper transitioning to red hues (Fig. S9). These results collectively demonstrate that GOx-FA-Mn NR mediate glucose decomposition into gluconic acid and H_2O_2, creating a self-amplifying system for enhanced CDT efficacy.

The production of ˙OH was validated using methylene blue (MB) as a probe. As demonstrated in Fig. 2e, the addition of FA-Mn NR with H_2O_2 resulted in a significant decrease in MB absorption, confirming effective ˙OH generation. Notably, GOx-FA-Mn NR displayed superior catalytic performance, functioning as a self-sufficient ˙OH generator through its integrated glucose oxidase—producing ˙OH even without exogenous H_2O_2 (Fig. 2f). To rigorously exclude non-specific oxidation interference, we implemented control groups without nanoparticles. These controls demonstrated no significant methylene blue degradation, confirming that ˙OH generation depends on nanoparticle-catalyzed Fenton-like reaction (Fig. S10). These results collectively validate the robust Fenton-like catalytic activity and efficient ˙OH generation capacity of the Mn(III)-doped nanoplatform.

Effects of Mn(III)-doped nanoparticles on cellular oxidative stress

Intracellular redox homeostasis is crucial to tumor cell survival and proliferation. Given the demonstrated ability of Mn(III)-

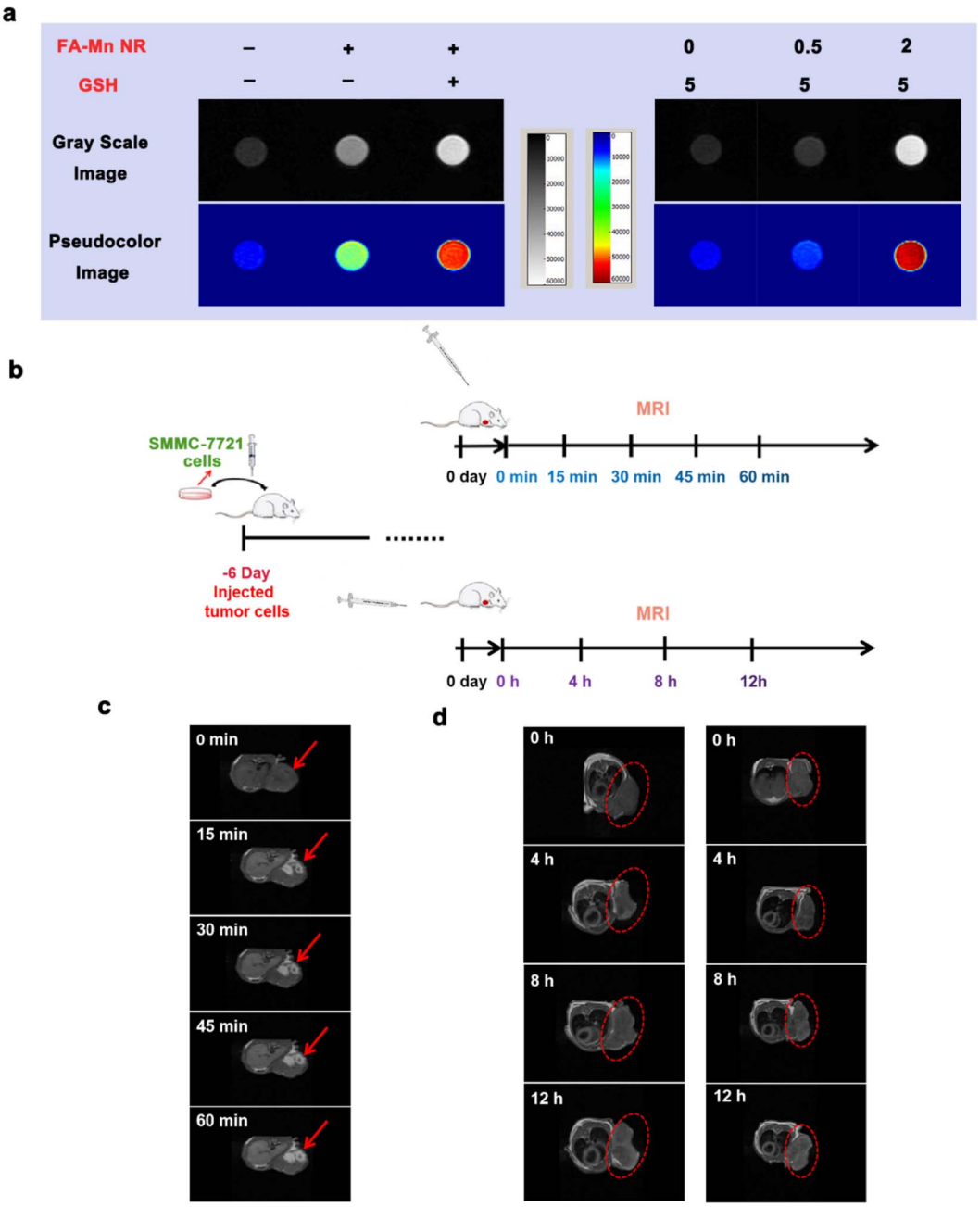

Fig. 4 MRI contrast performance. (a) MRI signals of FA-Mn NR with/without GSH. (b) Schematic of tumor MRI monitoring. (c) *In vivo* MRI in tumor sites after intratumoral injection with Mn NR. (d) *In vivo* MRI in tumor after intravenous injection with FA-Mn NR.

doped nanoparticles to generate $^{\bullet}OH$ in chemical systems, we further investigated the capacity to induce oxidative stress in tumor cells. The commercial probe DCFH-DA was used to evaluate the ability of nanoparticles to generate ROS in cells. DCFH-DA can cross the cell membrane and be hydrolyzed by intracellular esterase to produce non-fluorescent DCFH. Intracellular ROS oxidizes DCFH into fluorescent DCF to reflect intracellular ROS levels. As shown in Fig. S11 and S12, cells treated with Mn(III)-doped nanoparticles exhibited enhanced green fluorescence, indicating significant ROS accumulation. Notably, GOx-FA-Mn NR-treated cells demonstrated significantly stronger fluorescence signals, suggesting synergistic ROS amplification through GOx-mediated glucose decomposition and subsequent endogenous H_2O_2 production for Fenton-like reactions (Fig. 3a). In addition, flow cytometry analysis of thousands of cells further corroborated the conclusion. These results conclusively demonstrate that Mn(III)-doped nanoparticles disrupt cellular redox homeostasis *via* ROS generation, improving the efficacy as CDT agents.

Evaluation of cell death induced by Mn(III)-doped nanoparticles

Subsequently, the CDT effects of Mn(III)-doped nanoparticles were assessed *via* confocal fluorescence imaging using FITC-

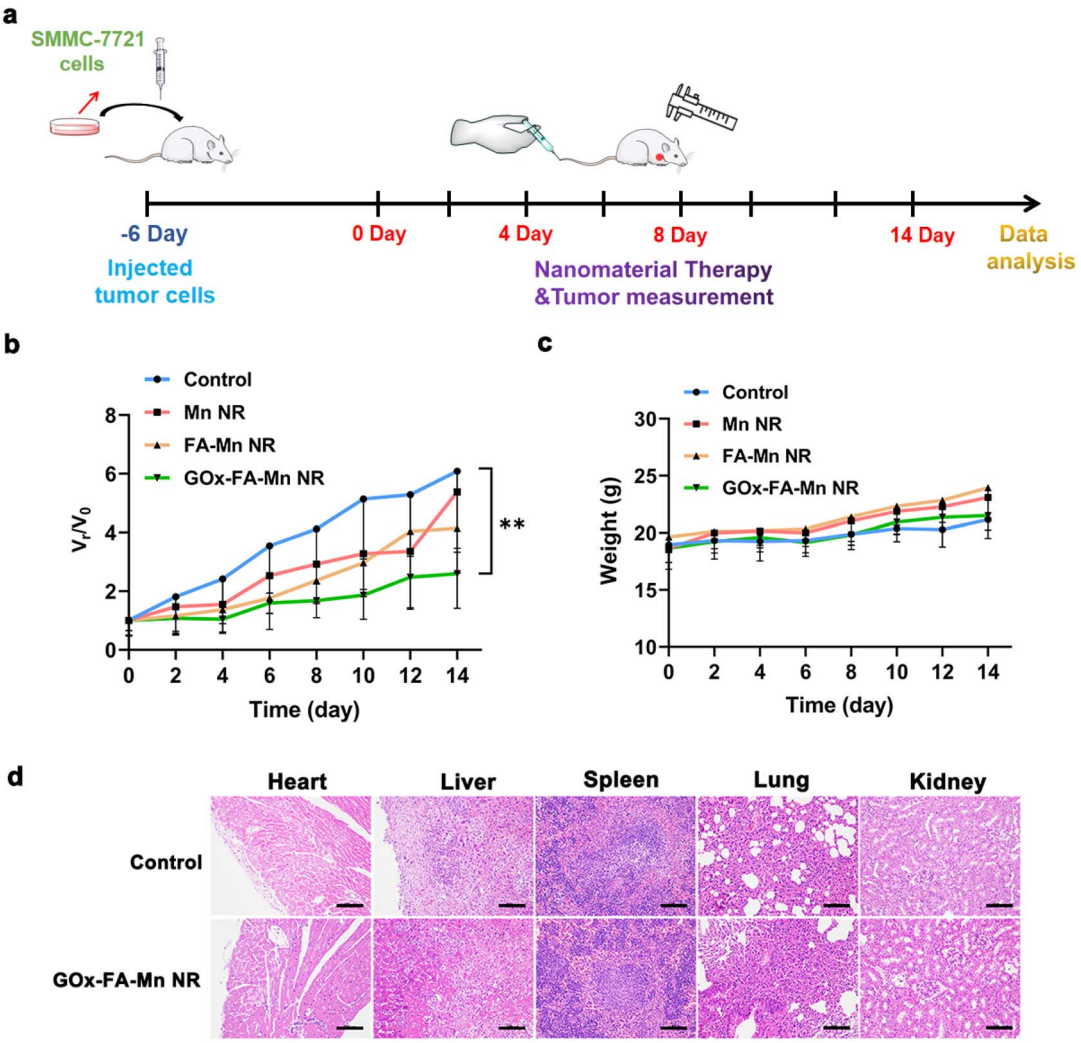

Fig. 5 *In vivo* antitumor efficacy. (a) Schematic diagram of tumor xenotransplantation and antitumor study. (b) The tumor volume of mice. (c) The weight of mice. (d) H&E-stained major organ sections after different treatments. Scale bar: 100 μm. Data are expressed as the mean ± SD. $^{**}p < 0.01$. The significance was determined by a Student's *t*-test.

Annexin V/PI staining (Fig. 3b). Cells treated with Mn NR or FA-Mn NR exhibited green fluorescence (FITC-Annexin V) with negligible red fluorescence (PI), indicative of early-stage apoptosis. Moreover, GOx-FA-Mn NR incubated cells showed strong green and red fluorescence, indicating that more cells were in the apoptotic stage. The results were quantitatively confirmed by flow cytometry analysis of >5000 cells per experimental condition, conclusively demonstrating the enhanced therapeutic potential of the GOx-integrated nanoplatform (Fig. 3d and S13).

To further quantitatively evaluate therapeutic efficacy, we performed MTT assays to assess different nanoparticle cytotoxicity. The results revealed concentration-dependent cytotoxicity for FA-Mn NR (Fig. 3c). When the concentration of FA-Mn NR was 75 μg mL^{-1}, the cell survival rate was about 50%. Notably, GOx-FA-Mn NR exhibited significantly enhanced cytotoxicity, reducing cell viability to ~20% at equivalent concentrations. This enhancement is attributed to GOx-mediated H_2O_2 supplementation, which amplifies Mn(II)-driven Fenton-like reactions. Collectively, these results demonstrate that GOx-FA-Mn NR synergize starvation therapy and CDT to achieve potent anti-tumor efficacy.

GSH-responsive MRI contrast performance

MRI remains indispensable for clinical diagnostics, providing deep-tissue resolution without optical limitations. As Mn^{2+} is a typical T_1 contrast agent, we systematically evaluated the imaging potential of Mn(III)-doped nanoparticles. Considering that the reaction between Mn(III) and GSH may affect the magnetic resonance imaging of nanoparticles, the magnetic resonance imaging signals in the system with and without GSH were investigated. As shown in the Fig. 4a, nanoparticle concentration-dependent signal enhancement was observed in GSH-containing systems. T_1 relaxation rate (r_1) measurements revealed a 2.1-fold increase (from 3.93 to 8.18 mM^{-1} s^{-1}) in relaxivity for FA-Mn NR following GSH exposure, demonstrating

the potential of FA-Mn NR as a GSH-responsive T_1 contrast agent (Fig. S14).

To assess *in vivo* imaging capability, we established SMMC-7721 tumor xenografts in BALB/c nude mice *via* subcutaneous cell inoculation. Following nanoparticle administration, magnetic resonance imaging was performed at designated time points (Fig. 4b). The experimental results showed that MRI signals appeared 15 min after intratumoral injection of Mn NR. In addition, the same results were confirmed in mice administered intravenously with FA-Mn NR. In detail, FA-Mn NR was administered intravenously to tumor-bearing mice for imaging at different intervals. Given that it takes time for the nanoparticles to travel through the bloodstream to reach the tumor and react with GSH, MRI was performed on the mice every four hours after injection. MRI signals became detectable in tumor regions 4 hours post-injection (Fig. 4c), demonstrating tumor-targeting capability and GSH-responsive contrast generation. The MRI performance of Mn(III)-doped nanoparticles can not only enable tumor lesions visualization, but also assess the distribution of CDT reagents during therapy, providing critical feedback for treatment optimization.

In vivo antitumor efficacy of Mn(III)-Doped nanoparticles

The therapeutic potential of GOx-FA-Mn NR was evaluated in SMMC-7721 tumor-bearing BALB/c nude mice. Tumor-bearing mice were randomized into four groups and systemically administered designated formulations every other day (Fig. 5a). Tumor volumes were monitored over a 14 days period to assess therapeutic outcomes.

Compared to the control group, all treatment groups exhibited tumor growth inhibition. Specifically, tumor size was slightly reduced in the Mn NR and FA-Mn NR groups (Fig. 5b). GOx-FA-Mn NR showed remarkable tumor growth inhibition, compared with the other groups, demonstrating superior therapeutic efficacy. Notably, no significant body weight fluctuations were observed across groups (Fig. 5c), confirming the systemic biocompatibility of Mn(III)-doped nanoparticles. To further demonstrate the effect of GOx-FA-Mn NR on other tissues *in vivo*, we performed H&E staining on tumor tissues (Fig. 5d). Compared with the control group, there was no abnormal damage in GOx-FA-Mn NR group, indicating that Mn(III)-doped nanoparticles have low toxicity to normal tissues. In conclusion, Mn(III)-doped nanoparticles have significant potential to inhibit tumor growth. Overall, while FA-Mn NR demonstrates reduced systemic toxicity, challenges remain for clinical application. GSH-activated systems inherently spare normal tissues with low glutathione levels, developing tumor-selective therapeutics remains challenging due to organ-specific GSH heterogeneity. Moreover, the results reveal a discrepancy between *in vivo* antitumor outcomes and *in vitro* cytotoxicity. This divergence is possiblely attributed to tumor microenvironmental constraints and heterogeneous nanoparticle distribution.[37,38] These results underscore the need for both therapeutic dosage optimization and comprehensive long-term safety evaluation to facilitate clinical translation. The FA-Mn NR as a promising theranostic platform provide critical guidance for developing next-generation platforms, suggesting that future systems incorporating microenvironmental triggers and improved tumor penetration capabilities may better overcome translational barriers.

Conclusions

Tumor redox homeostasis plays a pivotal role in regulating cancer cell proliferation, invasion, and metastasis. The unique tumor microenvironment simultaneously presents opportunities and challenges for both imaging and therapeutic intervention. Real-time monitoring of chemodynamic therapy agent distribution and metabolism within the TME could enable personalized treatment optimization. Here, we developed GSH-responsive Mn(III)-doped nanoparticles for MRI-monitored CDT. Comprehensive experimental validation established FA-Mn NR as a multifunctional theranostic platform with three key merits: (i) GSH depletion: disrupts tumor antioxidant defenses by depleting intracellular GSH *via* Mn(III)/Mn(II) redox cycling; (ii) imaging-guided therapy: Mn^{2+} released during GSH activation serves dual roles as MRI contrast agent and a Fenton-like catalyst for localized $^{\bullet}OH$ generation; (iii) synergistic functionality: integration of functional units such as GOx enables self-supplied H_2O_2 for enhanced CDT while initiating glucose deprivation-induced starvation therapy. Through a straightforward synthesis protocol, we engineered Mn(III)-doped nanoparticles capable of modulating tumor redox microenvironment and delivering potent anti-tumor effects. This work has optimized CDT-MRI systems by synergistically integrating folic acid targeting, GOx-mediated self-supplied H_2O_2, and Mn^{2+}-catalyzed $^{\bullet}OH$ amplification. The multifunctional design enables self-sustaining therapeutic cycles achieving independence from endogenous H_2O_2, thereby enhancing antitumor efficacy. The research establishes a paradigm for image-guided CDT, holding promise for addressing the urgent need for real-time therapeutic feedback. In the future, integrating MRI and other multimodal imaging techniques to develop precise tools for accurate tumor diagnosis and treatment guidance is important to the precise treatment. While future studies must address individual variability in dosing and response, our work provide a promising platform for MRI-monitored precision therapy.

Ethical statement

Animal experiments were conducted in accordance with relevant guidelines of the Chinese government and regulations for the care and use of experimental animals. All animal experiments were reviewed and approved by the Ethics Committee of Shandong Normal University, Jinan, P. R. China (approval number AEECSDNU2023063).

Author contributions

J. L., Z. J., W. Z., Y. T., and B. T. designed the experiments. J. L., Z. J., and X. C. performed the experiments. W. Z., P. L., Y. T., W. Z., H. W., and B. T. analyzed the results. All authors have given approval to the final version of the manuscript.

Conflicts of interest

The authors declare no conflict of interest.

Data availability

Supplementary information: All the data supporting this article have been included in the main text and the SI. See DOI: **https://doi.org/10.1039/d5sc04436g**.

Acknowledgements

This work was supported by National Natural Science Foundation of China (92253304, 22134004 and 22374091), Natural Science Foundation of Shandong Province (ZR2019JQ07 and 2021ZDSYS09). Local Science and Technology Development Fund Guided by the Central Government of Shandong Province (YDZX2022012).

Notes and references

1 N. Vasan, J. Baselga and D. M. Hyman, *Nature*, 2019, **575**, 299–309.
2 C. Y. Y. Yu, H. Xu, S. Ji, R. T. K. Kwok, J. W. Y. Lam, X. Li, S. Krishnan, D. Ding and B. Z. Tang, *Adv. Mater.*, 2017, **29**, 1606167.
3 C. Zhang, W. Bu, D. Ni, S. Zhang, Q. Li, Z. Yao, J. Zhang, H. Yao, Z. Wang and J. Shi, *Angew. Chem., Int. Ed.*, 2016, **55**, 2101–2106.
4 Z. Tang, Y. Liu, M. He and W. Bu, *Angew. Chem., Int. Ed.*, 2019, **58**, 946–956.
5 Y. Zhuang, S. Han, Y. Fang, H. Huang and J. Wu, *Coord. Chem. Rev.*, 2022, **455**, 214360.
6 Y. Han, J. Ouyang, Y. Li, F. Wang and J. Jiang, *ACS Appl. Mater. Interfaces*, 2020, **12**(1), 288–297.
7 Z. Yu, Q. Sun, W. Pan, N. Li and B. Tang, *ACS Nano*, 2015, **9**(11), 11064–11074.
8 Q. Sun, Z. Wang, B. Liu, F. He, S. Gai, P. Yang, D. Yang, C. Li and J. Lin, *Coord. Chem. Rev.*, 2022, **451**, 214267.
9 Y. Ma, C. Yan, Z. Guo, G. Tan, D. Niu, Y. Li and W. H. Zhu, *Angew. Chem., Int. Ed.*, 2020, **59**, 21143–21150.
10 J. V. Frangioni, *J. Clin. Oncol.*, 2008, **26**, 4012–4021.
11 C. Li, *Nature Mater.*, 2014, **13**, 110–115.
12 B. Ding, P. Zheng, F. Jiang, Y. Zhao, M. Wang, M. Chang, P. A. Ma and J. Lin, *Angew. Chem., Int. Ed.*, 2020, **59**, 16381–16384.
13 H. Li, Y. Liu, B. Huang, C. Zhang, Z. Wang, W. She, Y. Liu and P. Jiang, *Anal. Chem.*, 2022, **94**, 10470–10478.
14 F. Chen, X. Zhuang, L. Lin, P. Yu, Y. Wang, Y. Shi, G. Hu and Y. Sun, *BMC Med.*, 2015, **13**, 45.
15 D. Hanahan and R. A. Weinberg, *Cell*, 2011, **144**, 646–674.
16 G. K. Balendiran, R. Dabur and D. Fraser, *Cell Biochem. Funct.*, 2004, **22**, 343–352.
17 L. Kennedy, J. K. Sandhu, M. E. Harper and M. Cuperlovic-Culf, *Biomolecules*, 2020, **10**, 1429.
18 H. Sies, *Free Radical Biol. Med.*, 1999, **27**, 916–921.
19 D. M. Townsend, K. D. Tew and H. Tapiero, *Biomed. Pharmacother.*, 2003, **57**, 145–155.
20 E. Hatem, N. E. I. Banna and M. E. Huang, *Antioxid. Redox Signaling*, 2017, **27**, 1217–1234.
21 X. Guo, Y. Cheng, X. Zhao, Y. Luo, J. Chen and W. En Yuan, *J. Nanobiotechnol.*, 2018, **16**, 74.
22 H. J. Forman, H. Zhang and A. Rinna, *Mol. Aspects Med.*, 2009, **30**, 1–12.
23 W. Xuan, Y. Xia, T. Li, L. Wang, Y. Liu and W. Tan, *J. Am. Chem. Soc.*, 2020, **142**, 937–944.
24 J. M. Estrela, A. Ortega and E. Obrador, *Crit. Rev. Clin. Lab. Sci.*, 2006, **43**, 143–181.
25 X. Cheng, H. D. Xu, H. H. Ran, G. Liang and F. G. Wu, *ACS Nano*, 2021, **15**(5), 8039–8068.
26 L. S. Lin, J. Song, L. Song, K. Ke, Y. Liu, Z. Zhou, Z. Shen, J. Li, Z. Yang, W. Tang, G. Niu, H. H. Yang and X. Chen, *Angew. Chem., Int. Ed.*, 2018, **57**, 4902–4906.
27 S. S. Wan, Q. Cheng, X. Zeng and X. Z. Zhang, *ACS Nano*, 2019, **13**(6), 6561–6657.
28 Z. Zhou, H. Liang, R. Yang, Y. Yang, J. Dong, Y. Di and M. Sun, *Angew. Chem., Int. Ed.*, 2022, **61**, e202202843.
29 W. Xie, Y. Gan, L. Wang, Y. Si, Q. Li, T. Song, P. Wei, Z. Wu and G. Zhang, *Small*, 2024, **20**, 2306446.
30 A. D. Bokare and W. Choi, *J. Hazard. Mater.*, 2014, **275**, 121–135.
31 Z. Tang, P. Zhao, H. Wang, Y. Liu and W. Bu, *Chem. Rev.*, 2021, **121**, 1981–2019.
32 Z. Zhao, X. Wang, Z. Zhang, H. Zhang, H. Liu, X. Zhu, H. Li, X. Chi, Z. Yin and J. Gao, *ACS Nano*, 2015, **9**(3), 2749–2759.
33 X. Q. Wang, F. Gao and X. Z. Zhang, *Angew. Chem., Int. Ed.*, 2017, **56**, 9029–9033.
34 J. Noh, B. Kwon, E. Han, M. Park, W. Yang, W. Cho, W. Yoo, G. Khang and D. Lee, *Nat. Commun.*, 2015, **6**, 6907.
35 H. Wang, Z. He, Y. Yang, J. Zhang, W. Zhang, W. Zhang, P. Li and B. Tang, *Chem. Sci.*, 2019, **10**, 10876.
36 Z. Yu, P. Zhou, W. Pan, N. Li and B. Tang, *Nat. Commun.*, 2018, **9**, 5044.
37 T. He, H. Xu, Y. Zhang, S. Yi, R. Cui, S. Xing, C. Wei, J. Lin and P. Huang, *Theranostics*, 2020, **10**, 1544–1554.
38 L. H. Fu, C. Qi, Y. R. Hu, J. Lin and P. Huang, *Adv. Mater.*, 2019, **31**, 1808325.